A Composite Mesoscale Cumulonimbus Budget

A. K. BETTS

Dept. of Atmospheric Science, Colorado State University, Fort Collins 80521

(Manuscript received 12 October 1972)

ABSTRACT

Composite maps at levels from 950 to 150 mb of relative wind field ($\mathbf{v}_r$), mixing ratio (r), equivalent potential temperature (θ_E), and temperature perturbation (T') from the growth and decay phases of a mean mesoscale cumulonimbus system (systems used had a maximum radar echo area >400 km²) were constructed using radar and one rawinsonde (experiment VIMHEX) for days having a similar synoptic-scale wind field. Echo area and track were measured from radar film, and relative winds calculated by subtracting a mean echo velocity; positions of radiosonde data points relative to the echo as center were computed, scaled by an echo radius, and plotted with echo motion vectors aligned along one coordinate axis. Mass flows into the mean system at all levels give vertical mass transports for growth and decay phases, and net mass balance. The net convergence of r closely balances a mean surface rainfall per echo, and the net enthalpy source by the cumulonimbus system. Fluxes of θ_E into and out of the system for 5K ranges confirm energy conservation, and give updraft, downdraft transports. The vertical structure of net mass r and θ_E fluxes are presented. The mesoscale results are related to the large-scale modification of the mean atmosphere, using a theoretical cumulonimbus model. The large-scale vertical motion is computed as a residual from the temperature and water vapor budgets. Suitably averaged, the synoptic-scale mass transport is similar but not identical to the (life-cycle mean) cumulonimbus vertical mass transport. It is concluded that parametric models of cumulonimbus convection in terms of mass transport are quite realistic for these data above the lowest 150 mb, where the effects of horizontal variations between updraft and downdraft are dominant. The precise relationship between synoptic-scale controls and cumulonimbus-scale mass transport remains unclear.

1. Introduction

The vertical transports by deep convection (cumulonimbus convection) present a formidable problem to the understanding and modeling of the tropical atmosphere. The releases of latent heat are large, and the vertical redistribution of enthalpy and water vapor is very significant in determining the structure and time development of the mean atmosphere. At the same time deep convection can be regarded as a response to the large-scale thermodynamic fields, which in turn result from the large-scale horizontal and vertical motion fields. The atmospheric stratification is a subtle balance between large-scale forcing (e.g. mean vertical motion) and convective heat inputs and transports. Changes in mean atmosphere structure are thus smaller residuals of two larger opposing terms. Since we require these net changes, the details of the cumulonimbus-induced changes must be well understood. This is not an easy task, theoretically or observationally.

To obtain a four-dimensional data set on the mesoscale (10–100 km), adequate to resolve the structure and time development of a cumulonimbus system, though becoming feasible, is costly. During the first Venezuelan International Meteorological and Hydrological Experiment (VIMHEX I, 1969; H. Riehl, director) an attempt was made to deduce a mean structure for a mesoscale cumulonimbus system (area >400 km²) using the simplest possible technique: one 10-cm radar and a single rawinsonde station. The results, discussed in this paper, were encouraging. By carefully compositing data from many different days and storms, it was possible to construct maps for the flow into and around a mean storm at all pressure levels from the surface to above the outflow for both the growth and decay phases. Budget calculations on this mean system will be presented, and interpreted on the synoptic scale, using a simplified model for a cumulonimbus.

2. Data collection and analysis

a. Radar

A modified M-33 10-cm radar was located at Anaco in northeastern Venezuela for four months, June to September, 1969. The radar was scanned at successive elevation increments of 2° to its maximum elevation angle of 18°, and the PPI display was photographed with a 35-mm camera at attenuations of 0, 6, 12 and 18 db. This sequence of operations was repeated approximately every 15 min when echoes were visible. Using a microfilm reader, positions of major echos were traced, and echo area and heights calculated. Only

TABLE 1. Mean echo statistics.

Mean echo radius R	12.5 km
Mean echo growth time τ	66 min
Mean echo decay time τ	66 min
Mean echo travel speed	7 m sec^{-1}

The mean echo area (A_0) was taken as 500 km^2 and the area (A_R) scanned by the radar (working radius 80 km) as 20,000 km^2.

systems which reached a maximum area >400 km^2 were used to construct composites. The definition of a mesoscale system, often clusters of smaller cumulonimbus cells, clearly introduces some subjectivity: the radar analysis is discussed further in Cruz (1973). A mean velocity vector of an echo was calculated from the beginning and end of the trajectory. From the time sequence of echo area and height, a growth and decay phase for each echo could be defined with little ambiguity. Statistics for the mean echo were computed from a total of about 230 echos for the experiment period (Cruz, 1973). Some of these are shown in Table 1.

b. Rawinsonde

Before, during and after the period of deep convective activity, rawinsonde ascents were made adjacent to the radar at a time frequency initially of 2 hr, and later in the experiment of 1 hr. The strip chart data was tabulated at 1-min intervals and interpolated to specified pressure levels (at 25- or 50-mb intervals). It was found that the hygristor (Type ML-476) suffered from serious error in direct sunshine (see, e.g., Morrissey and Brousaides, 1970), and some correction was essential. A temperature difference independent of height between hygristor and thermistor was assumed, and a value deduced by comparing the surface relative humidity recorded by the radiosonde (extrapolated where necessary) with an accurate surface value obtained simultaneously with an aspirated psychrometer. This simple correction eliminates the major systematic error in the lowest levels [for further details, see Betts (1972)]. Fortunately, about half the data obtained during disturbed conditions were after sunset or under stratiform cloud, when the hygristor error is relatively small. Humidity values obtained before the period of deep convection under strong sunshine are less reliable as the correction is large (~4 gm kg^{-1}).

c. Construction of composite

The balloon position relative to a storm was calculated for each pressure level, and the coordinate system of each observation rotated so that all storm motion vectors were aligned along the positive X axis. The distance of the rawinsonde to the echo was also scaled by an echo radius measured along the line to the rawinsonde. The result of this simple scaling is that with echo radius unity, all data points within the unit circle were taken within the radar echo, while those at greater radii were outside the echo. Some scaling of distance is essential to compensate for different echo sizes: the procedure used here does not preserve divergence, but was chosen for simplicity. Wind velocities ($\mathbf{v}_r$) relative to the storm were calculated by subtracting the storm mean velocity vector at all levels, and maps were plotted of $\mathbf{v}_r$, equivalent potential temperature θ_E, mixing ratio r, and a temperature perturbation T', at pressure levels of 950, 900, 850, 800, 700, 600, 500, 400, 300, 250, 200, 175 and 150 mb. The temperature perturbation was defined near the surface (850–950 mb) as the difference between the deviation from the morning (0800) sounding, and a mean diurnal curve (with zero also at 0800) constructed from all the soundings. At higher levels a simple temperature difference from the last sounding preceding the onset of deep convection was taken. This apparently elaborate procedure is necessary since the synoptic and, at low levels, diurnal temperature variations are as large as the changes produced locally by the convection. Indeed the two can only be partially resolved. Humidity perturbation maps were not constructed because the water vapor measurements were of less basic accuracy. Composite maps were constructed for the growth and decay phases of a mean system for specific synoptic classifications.

d. Synoptic classification

To construct a composite mesoscale wind field around a cumulonimbus system, it is necessary for the synoptic-scale wind fields of different days to be comparable. Three attempts at classification using the synoptic wind fields over Venezuela and the Caribbean, at 850 and 200 mb, were made:

(i) By thermal structure—thickness 850 to 200 mb, warm or cold core.
(ii) By vorticity difference—850 to 200 mb.
(iii) By 850- and 200-mb winds relative to mean echo motion for that day.

The third classification was most successful; the others are less closely related to the wind field relative to an echo. Composite maps were therefore constructed for days with comparable high- and low-level synoptic-scale wind fields relative to a mean storm motion vector for that day.

Only one synoptic class proved to have a large enough data sample for analysis—that in which the low-level flow was easterly, while the storms moved westward faster than the low-level flow so that the upper level flow had a westerly component. In the frame where the storm is stationary, the relative wind field is nearly two-dimensional, with inflow in the front at low levels, and outflow to the rear at high levels (175 mb).

Important data characteristics for this class of days are shown in Table 2.

TABLE 2. Data for days in composite analysis.

Number of days	17
Total number of echos	90
Total mean rainfall in echo area (mm)	101
Mean rainfall per day (mm)	5.9
Number of echos per day (N)	5.3
Mean rain period per day (Δt, hr)	6.7

e. Composite analysis

The mixing ratio, equivalent potential temperature, temperature perturbation, and streamline fields were analyzed at each level for the growth and decay phases. A full isotach analysis seemed less convincing, and in the light of the theoretical framework discussed in the next section, it was decided that only fluxes into and out of the echo could be calculated to useful accuracy.

The mean echo was considered enclosed in a cylindrical shell from the surface (990 mb) to 137.5 mb (see Fig. 1), with a non-dimensional radius $\hat{R}=2$ ($\hat{R}=1$ corresponds to the echo boundary). Fluxes across the vertical boundary of this cylinder were computed at the pressure levels from 950 to 150 mb: net vertical mass flux at 137.5 mb proved negligible. Examples of the analyzed fields are shown in Fig. 2.

1) MASS FLUX

Wind speeds were estimated from the rather scattered data at 12 equally spaced intervals on the circle $\hat{R}=2$. Radial velocities C_k ($k=1, \ldots, 12$) were calculated from wind speed and streamlines. Though the scatter in the individual data was considerable, the resulting net mass convergence varied uniformly with pressure (though in opposite senses) for growth and decay phases. Little re-analysis was necessary.

2) WATER VAPOR AND TEMPERATURE PERTURBATION

The mass convergence analysis was overlaid in turn on the analyzed fields of water vapor and temperature perturbation.

Net fluxes into the echo across the circle $\hat{R}=2$ were calculated using the 12 values of C_k and corresponding means r_k, T_k' for r, T', for each circumference interval.

3) EQUIVALENT POTENTIAL TEMPERATURE

The field of θ_E was treated differently from those of r, T'. In a precipitating system, the release of latent heat resulting from a net condensation of water vapor to liquid increases the enthalpy of the mean atmosphere. A budget on a cumulonimbus system may be regarded as conserving enthalpy plus latent heat on a scale of an hour or two.

It is convenient to use θ_E as a conserved quantity both to investigate this energy conservation, and to give a more detailed picture of the vertical transports (Rasmussen *et al.*, 1969). The usual definitions of θ_E involve approximations, e.g., the neglect of the specific heat of liquid water, and of the ice phase. Further, in isobaric mixing the volume integral $\int C_p \theta_E \rho dV$ (where ρ is air density and C_p the specific heat of dry air) is only approximately conserved (see, e.g., Betts, 1973). However, typical errors are about 5% and within the level of accuracy of this experiment.

The convergence analysis was overlaid on the θ_E analysis, and the net mass flux in 5K ranges of θ_E (from 330-355K) into the composite system was calculated.

f. Mean fields

The theoretical framework presented in the next section requires averages of T and r, outside the volume containing the echo. These were calculated as simple averages of the data values outside $\hat{R}=2$. More data points would be preferable to obtain a representative average, but this average is not critical. More critical are representative synoptic-scale averages of T, r before and after the period of deep convection, which are essential to interrelate mesoscale transports and the synoptic-scale motion field (Section 3). Mean values $\bar{T}(p)$ for 17 days on the data set (Table 2) were obtained by averaging the last sounding preceding the deep convection, and the soundings immediately afterward. The mean horizontal advection over these 17 days will be supposed negligible for the large-scale budget calculations.

Representative values of $\bar{T}(p)$ near the surface (990–850 mb) were not thought obtainable because of the large diurnal temperature change, and the widely varying time interval between the last sounding preceding the rain period, and the rain period itself.

Mean values $\bar{r}(p)$ after the deep convection were found similarly, but a mean sounding before could only be obtained by selecting from a much larger sample,

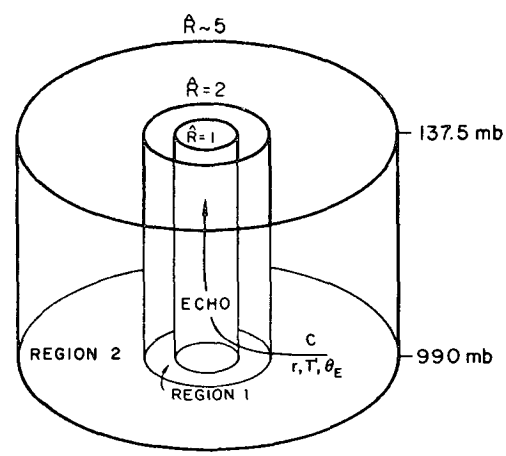

FIG. 1. Cumulonimbus model used for budget computations. Radius of 1, 2 boundary is twice that of echo.

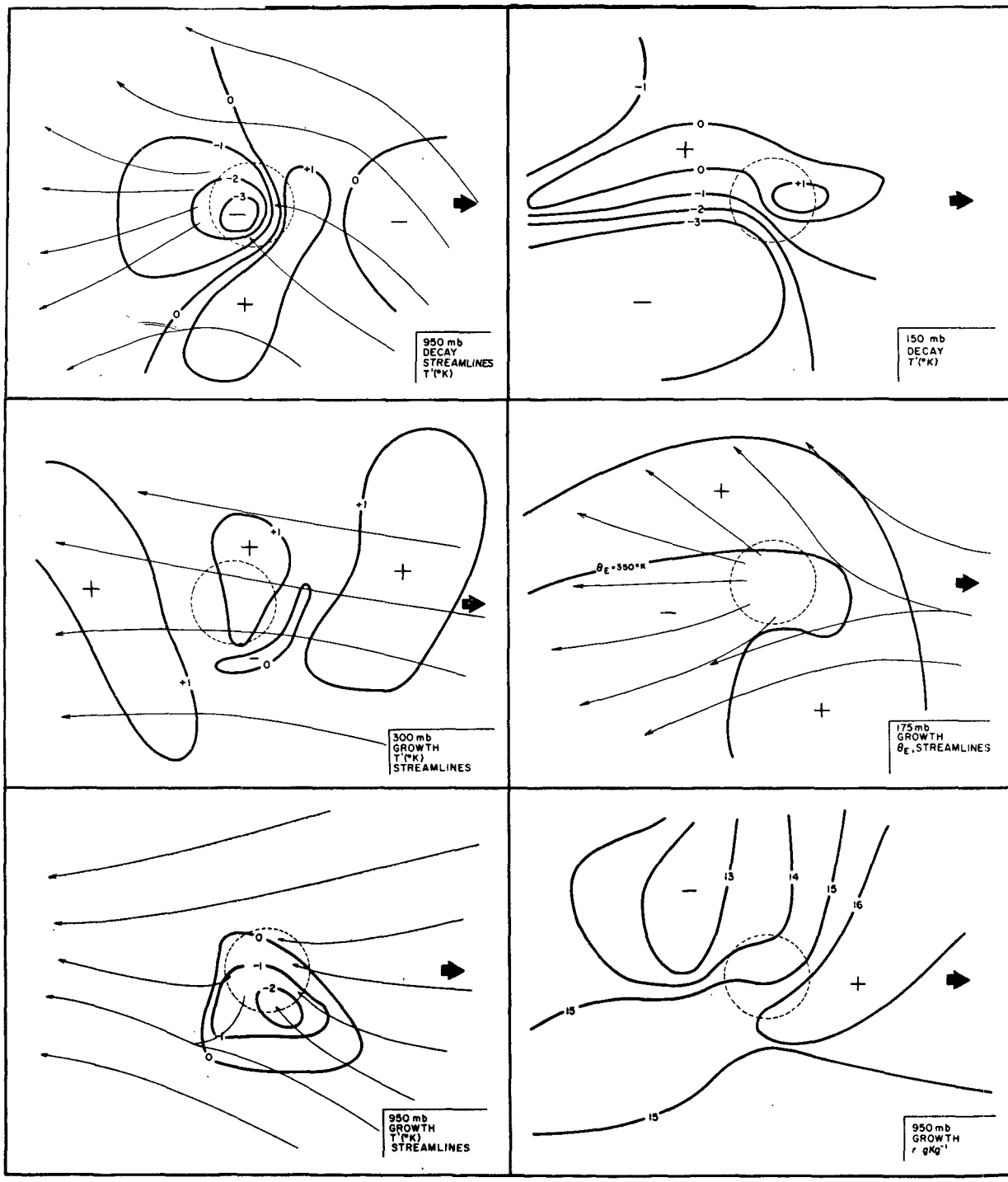

FIG. 2. Example mesoscale fields around a mean echo (diameter 25 km) at 950, 300 and 175 mb (growth) and at 950 and 150 mb (decay).

owing to the serious inaccuracies in the humidity sensor. The humidity errors are largest prior to a rain episode when solar radiation is large and cloud cover relatively small. The synoptic scale r budget is thus only indicative.

3. Theoretical model

a. Model description

The cylindrical shell $\hat{R}=2$ (see Fig. 1) separates the cloud region (horizontal area A_1) from its environment

(area A_2). The fluxes into the cylinder across the 1, 2 boundary were measured at pressure levels from 950–150 mb (see Sections 2e and 5), and the net vertical mass flux at 137.5 mb proved negligible (Section 5a). The area ratio of regions 1 to 2 is a time-space average and is discussed later in 4e. This model of cumulonimbus convection is an extension of those of Pearce and Riehl (1968) and Yanai (1971).

In region 2, potential temperature (θ) and water vapor will be considered conserved, that is, all the phase changes of water will be supposed to take place in region 1 (an area four times the mean echo area). Radiative fluxes have been omitted, since they are sensitive functions of a largely unknown distribution of cloud. Though not necessarily negligible, they are considerably smaller than the cumulonimbus heating on the measured time scale of 1–6 hr. Surface fluxes will also be neglected during the cloud lifetime.

b. Conservation equations[1]

The flux form of the conservation equation for a property Q is

$$\frac{\partial(\rho Q)}{\partial t}+\nabla\cdot(\rho \mathbf{v} Q)=0. \tag{3.1}$$

Eq. (3.1) can be integrated over both regions. Certain assumptions will be made in the budget equations, i.e., $\rho=\rho(p)$ only, $p=p(z)$ only (hydrostatic assumption), and a density-weighted vertical velocity will be defined as

$$\omega=-\rho g w.$$

Over region 1, after horizontal averaging and using the divergence theorem,

$$A_1\frac{\partial\tilde{Q}^1}{\partial t}+A_1\frac{\partial\widetilde{\omega Q}^1}{\partial p}+\int_{l_1} CQdl_1=0,$$

where l_1 is the length of the 1, 2 boundary, C the radial component of the horizontal wind (positive outward), and the tilde (before superscript 1) denotes an area average over region 1. Here we shall only use the above relation in region 1 for mass, for which $Q=1$. Hence,

$$\frac{\partial\tilde{\omega}^1}{\partial p}=-\frac{1}{A_1}\int_{l_1} Cdl_1, \tag{3.2}$$

$$A_1\tilde{\omega}^1=-A_1\rho g\tilde{w}^1=-\int_{990}^{p} dp\int_{l_1} Cdl_1, \tag{3.3}$$

with the surface boundary condition $\tilde{w}^1=0$. The surface pressure will be assumed constant at 990 mb. $A_1\tilde{\omega}^1$ is a cumulonimbus scale mass transport.

[1] Symbols are defined in the Appendix.

Similarly, over region 2

$$A_2\frac{\partial\tilde{Q}^2}{\partial t}+A_2\frac{\partial\widetilde{\omega Q}^2}{\partial p}-\int_{l_1} CQdl_1+\int_{l_2} CQdl_2=0, \tag{3.4}$$

where l_2 is the length of outer boundary of region 2. For mass, $Q=1$, and (3.4) reduces, using (3.2), to

$$\frac{\partial\tilde{\omega}^2}{\partial p}=-\frac{A_1}{A_2}\frac{\partial\tilde{\omega}^1}{\partial p}+\frac{A_1+A_2}{A_2}\frac{\partial\tilde{\omega}}{\partial p},$$

where $\tilde{\omega}$ is a large-scale average over both cloud and environment, related to the mass inflow across l_2.

Integrating, with $\tilde{\omega}^1=\tilde{\omega}^2=\tilde{\omega}=0$ at $p=990$ mb (the surface), we have

$$\tilde{\omega}^2=\frac{A_1+A_2}{A_2}\tilde{\omega}-\frac{A_1}{A_2}\tilde{\omega}^1. \tag{3.5}$$

For $A_1\ll A_2$, we note

$$\tilde{\omega}^2=\tilde{\omega}-f\tilde{\omega}^1,$$

where f is the fractional area $A_1/(A_1+A_2)$. The vertical p-velocity $\tilde{\omega}^1$ can be measured from the composite, so this will be taken as representative of the cloud mass circulation. An alternative definition exists: that of defining $\tilde{\omega}^1-\tilde{\omega}$ (the excess vertical mass flux over $\tilde{\omega}$ in region 1) as a measure of the cloud mass circulation. However, it could be argued that the latent heat release is related to $\tilde{\omega}^1$, rather than $\tilde{\omega}^1-\tilde{\omega}$; the difference, of course, is small since $\tilde{\omega}\ll\tilde{\omega}^1$.

For other properties $Q=\theta$, r, θ_E; and we make two further assumptions to simplify (3.4). We shall assume no vertical eddy transport in region 2 (the environment), i.e.,

$$\widetilde{\omega' Q'}^2=0,$$

a necessary approximation as we have no data on these transports. Clearly, the vertical eddy transports outside the cloud region are likely to be much smaller than inside, and the data show that fluxes across the 1, 2 boundary are nearly in hydrostatic balance, at least above a surface layer. We shall also neglect large-scale horizontal gradients and hence local changes by advection, by assuming $Q=\tilde{Q}^2$ on the outer boundary l_2. Eq. (3.4) can then be simplified to

$$A_2\frac{\partial\tilde{Q}^2}{\partial t}+A_2\tilde{\omega}^2\frac{\partial\tilde{Q}^2}{\partial p}-\int_{l_1} C(Q-\tilde{Q}^2)dl_1=0. \tag{3.6}$$

The last term includes an "eddy" flux across the 1, 2 boundary through the correlation of C and Q. (If $Q=\tilde{Q}^2$ on the 1, 2 boundary, then the last term is zero.)

Using (3.5), we then have

$$A_2\frac{\partial\tilde{Q}^2}{\partial t}=-[(A_1+A_2)\tilde{\omega}-A_1\tilde{\omega}^1]\frac{\partial\tilde{Q}^2}{\partial p}+\int_{l_1}C(Q-\tilde{Q}^2)dl_1. \quad (3.7)$$

In typical cases both the right-hand terms are residuals. The data will show that, in the middle atmosphere where vertical motions are large, the first term (derived from $\tilde{\omega}^2$) is dominant, while at the surface and above the main outflow, the last term becomes dominant.

c. Further derivations

By integrating over a cloud-life cycle, one may suppose that the area mean change is well approximated by that in region 2, i.e.,

$$\frac{\partial\tilde{Q}^2}{\partial t}=\frac{\partial\tilde{Q}}{\partial t}. \quad (3.8)$$

This is valid if

$$\frac{A_1}{A_1+A_2}\frac{\partial}{\partial t}(\tilde{Q}^1-\tilde{Q}^2)\ll\frac{\partial}{\partial t}\tilde{Q}^2,$$

which is likely to be a reasonable approximation for $A_1/(A_1+A_2)\approx 10\%$. However, this may be a better approximation for θ (as the atmosphere is never far from hydrostatic balance), than for r. Using the rawinsonde data of this experiment, $\tilde{Q}^2$ and $\tilde{Q}$ cannot be accurately distinguished, either in their time or pressure derivatives. Further, the storage change in region 1 [assumed in (3.8)] is negligible when pressure-integrated, compared with the fluxes across the 1, 2 boundary. Using (3.8), Eq. (3.7) becomes

$$\frac{A_2}{A_1+A_2}\frac{\partial\tilde{Q}}{\partial t}=-\left[\tilde{\omega}-\frac{A_1}{A_1+A_2}\tilde{\omega}^1\right]\frac{\partial\tilde{Q}^2}{\partial p}+\frac{1}{A_1+A_2}\int_{l_1}C(Q-\tilde{Q}^2)dl_1. \quad (3.9)$$

The factor $A_2/(A_1+A_2)$ in (3.9) is close to unity, and quantitatively rather trivial. It arises from the inclusion in $\tilde{\omega}^1$ of the large-scale $\tilde{\omega}$ over the area A_1.

One further transformation of (3.7) is important. Integrating over pressure, and using (3.2), we note

$$\int_{990}^{137.5}dp\left[A_1\tilde{\omega}^1\frac{\partial\tilde{Q}^2}{\partial p}-\int_{l_1}C\tilde{Q}^2dl_1\right]=A_1[\tilde{\omega}^1\tilde{Q}^2]_{990}^{137.5}\equiv 0;$$

therefore,

$$\frac{A_2}{A_1+A_2}\int_{990}^{137.5}\frac{\partial\tilde{Q}^2}{\partial t}dp=-\int_{990}^{137.5}\tilde{\omega}\frac{\partial\tilde{Q}^2}{\partial p}dp+\frac{1}{A_1+A_2}\int_{990}^{137.5}dp\int_{l_1}CQdl_1. \quad (3.10)$$

The pressure-integrated modification outside the echo region may be expressed in terms of a large-scale term, and an exchange with the echo region, where Q may not be conserved. If $Q=\theta$, the last term represents a large input, since the mass divergence is at a higher θ than the convergence.

If $Q=r$, this term is a large sink of water vapor, which falls out as rain if there is no change in storage inside region 1.

If $Q=\theta_E$, then the last term is zero to the extent that θ_E integrated over mass is conserved in the wet process and that there is no storage change inside region 1. Thus, the pressure-integrated local mean change of θ_E can be calculated from the large-scale $\tilde{\omega}$.

It should be stressed that Eq. (3.7) [or (3.9)] is the equation for computing local changes at a pressure level—not the terms under the pressure integral on the right-hand side of (3.10).

4. Evaluation

a. Mass

Eq. (3.3) was evaluated using 12 values of C, equally spaced on the circumference l_1 at $\hat{R}=2$ (see Section 2e), and pressure increments Δp between the half-way points between pressure levels. A few pressure increments, therefore, have uncentered values, but the data accuracy does not warrant an interpolation scheme. Vertical fluxes were computed using echo area A_0 as a standard area, rather than A_1 (the inner cylinder cross section). This does not affect the integrated vertical transport in region 1, and was done on the basis that the bulk of the vertical transport is probably within the echo, and vertical velocities so computed are more illuminating than if based on the arbitrary cylinder at $\hat{R}=2$; i.e.,

$$A_0\omega^*=A_1\bar{\omega}^1, \quad (4.1)$$

where $A_0=A_1/4$, and the overbar represents the composite mean [a 17-day mean (see Table 2) as well as an areal mean]. After substituting (4.1), Eq. (3.3) in finite-difference form becomes

$$-\omega^*(p_s)=\frac{1}{3R}\sum_{i=1}^{s}\Delta p_i\sum_{k=1}^{12}C_{ki}, \quad (4.2)$$

since the increment of circumference $\Delta l=4\pi R/12$ and the chosen reference area is πR^2.

In the tabulations and graphs, values of $\sum C_k$ and ω^* for the growth and decay phases, which had *equal* duration, will simply be added to give the total life-cycle transport. This means that the reference time period for computing the total transport by the composite system over its life cycle is the half lifetime: $\tau = 66$ min (Table 1).

b. Water vapor

The convergence of water vapor (see Section 2e) into the system at a level is

$$\frac{\pi R\tau}{3g}\Delta p_i \sum_L \sum_k C_{ki} r_{ki}, \tag{4.3}$$

where $\sum_L$ is to be interpreted as summing over the lifetime, i.e., both growth and decay phases.

c. Equivalent potential temperature

The vertical velocity was computed for each 5K range of $\theta_E[\theta_{Ej}]$ using the form

$$-\omega^*(p_s,\theta_{Ej}) = \frac{1}{3R}\sum_{i=1}^{s} \Delta p_i \sum_L \sum_k C_{kji}(\theta_{Ej}). \tag{4.4}$$

d. Temperature

Fields of temperature perturbation rather than potential temperature were plotted (see Section 2c). Letting Q be θ in (3.9), re-expressing in terms of T, T', and using a finite-difference form, one obtains [using (4.1)]

$$\frac{A_2}{A_1+A_2}\frac{\partial \overline{T}(p_i)}{\partial t} = -\left[\bar{\omega}(p_i) - \frac{A_0}{A_1+A_2}\omega^*(p_i)\right]\left[\frac{\overline{T}}{\bar{\theta}}\frac{\overline{\Delta\theta}^2}{\Delta p}\right]_i + \frac{\Delta l}{A_1+A_2}\sum_k C_{ki}(T'_{ki} - \overline{T'_i}^2). \tag{4.5}$$

The total enthalpy input by the echo, which can be compared to a latent heat release equivalent to the net vapor inflow (4.3), is

$$\frac{\pi R\tau C_p}{3g}\sum_i \left[-3R\Delta p_i \sum_L \omega^*(p_i)\left(\frac{\overline{T}\overline{\Delta\theta}^2}{\bar{\theta}\Delta p}\right)_i - \Delta p_i \sum_L \sum_k C_{ki}(T'_{ki} - \overline{T'_i}^2)\right]. \tag{4.6}$$

For convenience in (4.10) and Table 5, the two terms inside the brackets will be denoted E_1, E_2, respectively.

e. Meso-synoptic interaction

The modification of the mean atmosphere over the period of deep convection involves a time integration of (4.5) for the period Δt (Table 2). At each pressure level, dropping the i suffix, we thus have

$$\frac{A_2}{A_1+A_2}\Delta\overline{T} = -\left[\frac{\overline{T}}{\bar{\theta}}\frac{\overline{\Delta\theta}^2}{\Delta p}\right]\left[\bar{\omega}\Delta t - \frac{A_0}{2(A_1+A_2)}\Delta t\sum_L \omega^*\right] + \frac{\Delta t\Delta l}{2(A_1+A_2)}\sum_L \sum_k C_k(T'_k - \overline{T'}^2). \tag{4.7}$$

The area unit (A_1+A_2) per storm can be calculated from Table 2, using A_R (the radar area), N (the number of echoes per time period Δt in A_R), and 2τ (the echo lifetime), i.e.,

$$(A_1+A_2) = A_R\Delta t/2N\tau = A_R/n, \tag{4.8}$$

where n is the mean number of echoes visible in A_R at one time. Thus, for this 17-day sample, the average instantaneous area cover of echo during the period of deep convection is $2NA_0\tau/(A_R\Delta t) \approx 4\%$, but the average total area covered by echoes during the daily period of deep convection is $NA_0/A_R \approx 13\%$.

Using (4.8), Eq. (4.7) becomes

$$\frac{A_2}{A_1+A_2}\Delta\overline{T} = -\left[\frac{\overline{T}}{\bar{\theta}}\frac{\overline{\Delta\theta}^2}{\Delta p}\right]\left[\bar{\omega}\Delta t - \frac{A_0}{A_R}N\tau\sum_L \omega^*\right] + \frac{N\tau\Delta l}{A_R}\sum_L \sum_k C_k(T'_k - \overline{T'}^2). \tag{4.9}$$

Thus, both time and space averages are involved in comparing ω^* with $\bar{\omega}$. Eq. (4.9) can be written

$$\frac{A_2}{A_1+A_2}\Delta\overline{T} = \Delta T_{\bar{\omega}} + \Delta T_{Cb}, \tag{4.10}$$

where

$$\left.\begin{aligned}\Delta T_{\bar{\omega}} &= -\frac{\overline{T}\overline{\Delta\theta}^2}{\bar{\theta}\Delta p}\bar{\omega}\Delta t \\ \Delta T_{Cb} &= \frac{\pi RN\tau}{3A_R\Delta p}(E_1+E_2)\end{aligned}\right\}.$$

The analog of (4.9) for water vapor is

$$\frac{A_2}{A_1+A_2}\Delta\bar{r} = -\left[\frac{\overline{\Delta r}^2}{\Delta p}\right]\left[\bar{\omega}\Delta t - \frac{A_0}{A_R}N\tau\sum_L \omega^*\right] + \frac{N\tau\Delta l}{A_R}\sum_L \sum_k C_k(r_k - \overline{r}^2), \tag{4.11}$$

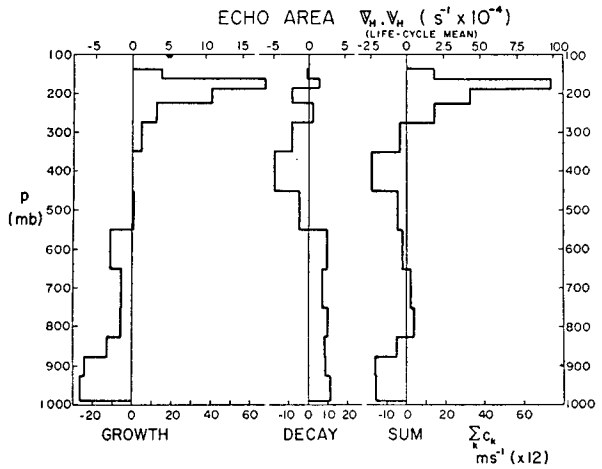

FIG. 3. Convergence (negative values) and divergence (positive values) into echo region 1 vs pressure for growth and decay phases, and for the net life cycle.

with corresponding definitions for $\Delta r_{\bar{\omega}}$, Δr_{Cb}, V_1, V_2, which will be used in Tables 7 and 8.

5. Results

a. *Mass budget*

The convergence and divergence as a function of pressure for the growth and decay phases, and their sum (representing the net convergence) are presented in Fig. 3 and Table 3, and the vertical mass flux curves in Fig. 4. Neither growth nor decay phases show strict mass balance, but the difference is within experimental error. Since the growth and decay phases lasted equal times (Table 1), the sum of their mass transports is the best estimate of the net transport over the life cycle of the system. This net mass budget shows mass balance, which simplifies the subsequent analysis. Though the net mass transport on the cumulonimbus scale is up at all levels, there is more structure than that corresponding to simple inflow at low levels and outflow at high levels. Referring to (4.5) it is clear that the slight decrease of the net ω^* from 800 to 600 mb will have important consequences on the synoptic-scale modification of the atmosphere, unless $\bar{\omega}$ has a corresponding profile.

It should be noted that even though the growth phase is dominated by updrafts and the decay phase by downdrafts, that even for each phase the vertical mass flux is the sum of upward and downward transports on the cumulonimbus scale. These can be resolved somewhat further using the θ_E analysis.

b. *Equivalent potential temperature budget*

The convergence, divergence patterns in 5K ranges of θ_E from 330–355K are shown in Fig. 5. In the two highest ranges, there is inflow at low levels and outflow at 200–175 mb, clearly a so-called "hot tower" transport (Riehl and Malkus, 1958). In the three lower

TABLE 3. Mass balance for growth and decay phases.

Pressure levels (mb)	p (mb)	$(-\Delta p_i)$ (mb)	Growth $\sum_k C_k$ (m sec^{-1})	Growth $(-\omega^*)$†	Decay $\sum_k C_k$ (m sec^{-1})	Decay $(-\omega^*)$	Sum $\sum_L \sum_k C_k$ (m sec^{-1})	Sum $(-\omega^*)$†
	990			0		0		0
950		65	−26.4		11.2		−15.2	
	925			46		−19		26
900		50	−24.2		8.8		−15.4	
	875			78		−31		48
850		50	−12.8		8.1		− 4.7	
	825			95		−42		53
800		75	− 5.9		9.9		4.0	
	750			107		−62		45
700		100	− 5.1		7.3		2.2	
	650			121		−81		40
600		100	−11.4		9.5		− 1.9	
	550			151		−107		45
500		100	0.3		− 4.6		− 4.3	
	450			150		−94		56
400		100	0		−17.8		−17.8	
	350			150		−47		104
300		75	4.8		− 8.2		− 3.4	
	275			141		−30		110
250		50	12.4		2.2		14.6	
	225			124		−33		91
200		37.5	40.6		− 8.2		32.4	
	187.5			84		−25		59
175		25	68.4		5.3		73.7	
	162.5			38		−29		10
150		25	15.0		− 0.9		14.1	
	137.5	(Residual)		28		−28		0

† In cgs units.

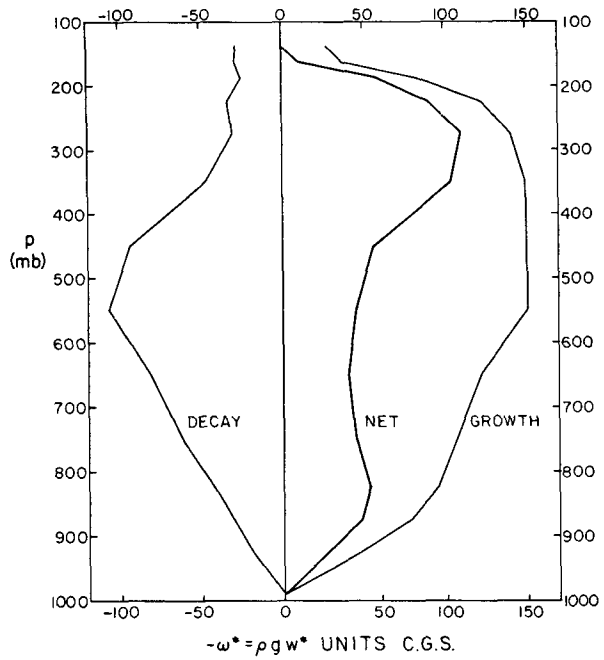

FIG. 4. Vertical mass flux ($-\omega^*$) vs pressure for growth and decay phases, and their sum (representing the net mass flux).

ranges, the transports are more complex, but clearly distinguishable is a downdraft flow in the lowest layers: convergence above and divergence below. In the mean system, downdrafts do not extend from the mid-troposphere to near the surface (these cumulonimbus systems are not as highly organized as some squall lines), but air typically is descending about 80 mb in downdrafts. However, one can produce a simpler model by summing the mass transport in the ranges 330–345K and 345–355K (Fig. 6). The result is a low θ_E downdraft between 400 mb and the surface, and a high θ_E updraft to 175 mb.

None of the individual θ_E ranges show exact mass balance but the residual is within experimental error. Furthermore, mixing processes could produce overlapping between the ranges, though this would tend to give negative residuals in the middle ranges and positive values at the extremes, not the pattern observed. The pattern of residuals is consistent with a storage change, increasing the mean θ_E inside the echo region (see Fig. 6). This is not unlikely although it is not confirmed by the energy balance presented in the next section. The analyses of T', r and θ_E were made independently, however, so some differences must be expected.

c. *Water vapor, rainfall and energy conservation*

The fluxes of water vapor into region 1 are shown in Table 4. The net vapor convergence into the system over the life cycle will be taken to equal the rainfall. This requires some justification. It is not being said that all the water condensed falls as rain, only that which is not re-evaporated in downdrafts. By taking the θ_E ranges 330–345K and 345–355K (see Fig. 6) one can distinguish updraft condensation and downdraft evaporation more closely. These are also given in Table 4, where the net convergence into the high θ_E updraft (a measure of the total condensation) is about twice the vapor divergence from the lower θ_E downdraft (a

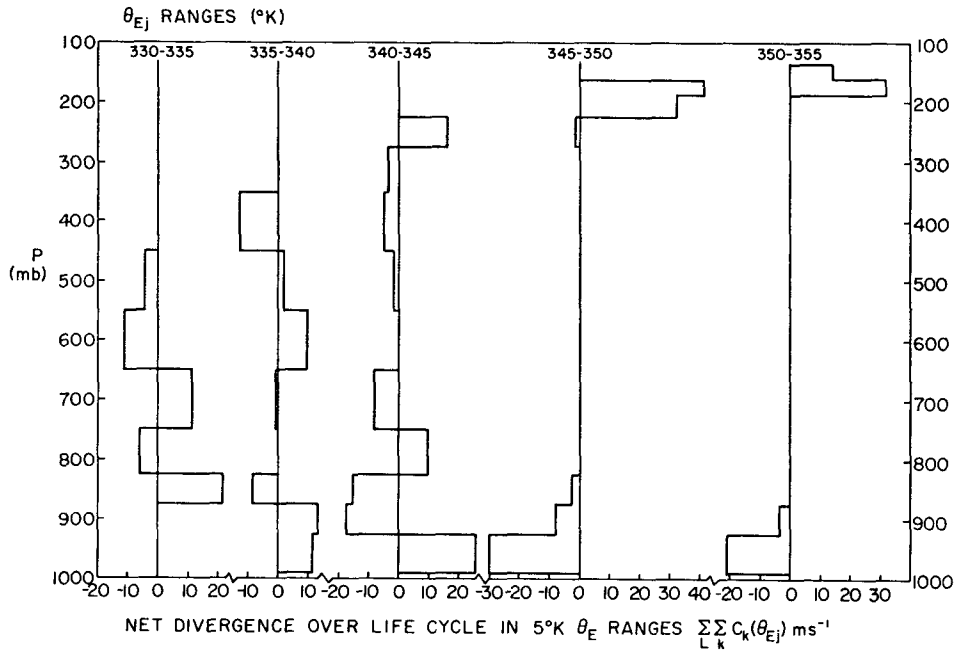

FIG. 5. Net life-cycle convergence, divergence patterns into echo region 1 vs pressure.

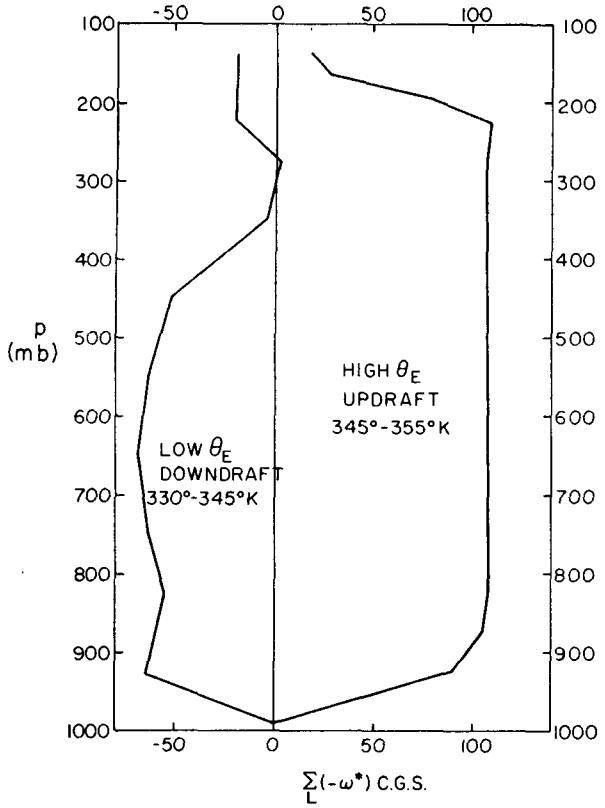

FIG. 6. Net vertical mass flux vs pressure for high (345–355K) and low θ_E (330–345K) ranges, depicting simplified updraft and downdraft.

measure of the re-evaporation). The total net vapor convergence into the composite echo is 1.83×10^{13} gm.

The total enthalpy input [Eq. (4.6)] by the cumulonimbus system can be calculated from the thermal fields, and compared with the net latent heat release if the net vapor convergence is condensed (i.e., no change in vapor storage in region 1). The results are given in Table 5. The composite echo is an enthalpy source of 1.08×10^{16} cal corresponding to a net condensation of 1.8×10^{13} gm of water, within a few percent of the net vapor convergence, and well within experimental error. Clearly, the net condensation in region 1 only equals the rainfall if there is also no change in storage of liquid water from growth to decay phase. Since there were no measurements of the total mean liquid water content of the atmosphere, this will be assumed.

The total net vapor convergence into the composite echo corresponds to 3.7 cm of rain over the echo area, during the echo lifetime. This can be compared with the measured mean rainfall per echo for the days in

TABLE 5. Energy conservation check [Eq. (4.6)].*

p (mb)	$\overline{T}^2$ (°C)	E_1	E_2	E_1+E_2
990	26.0			
950	23.6	41	−325	−284
900	20.4	206	−260	−54
850	17.2	382	−275	107
800	14.5	634	75	709
700	8.2	840	0	840
600	1.9	1000	220	1220
500	−6.0	1161	230	1391
400	−16.8	1728	10	1738
300	−31.8	1453	83	1536
250	−42.2	761	−20	741
200	−54.5	446	94	540
175	−61.5	248	−23	225
150	−68.1	49	−280	−231
	Σ	8949	−471	8478
	$\Sigma\times\frac{C_p}{L}$	3580	−190	3390**

* In units of 10 mb m sec^{-1} (°K). See (4.7) for definitions of E_1, E_2.

** The total of 3390 units is an enthalpy source of 1.08×10^{16} cal to be compared with vapor convergence of −3450 units.

TABLE 4. Water vapor balance.*

p (mb)	$(-\Delta p_i)$ (mb)	Growth $\sum C_k r_k$	Growth $(\Delta p_i)\sum C_k r_k$	Decay $\sum C_k r_k$	Decay $(-\Delta p_i)\sum C_k r_k$	Sum $\sum_L\sum C_k r_k$	Sum $(-\Delta p_i)\sum_L\sum C_k r_k$
950	65	−452	−2808	168	1092	−264	−1716
900	50	−346	−1730	75	375	−271	−1355
850	50	−165	−825	83	415	−82	−410
800	75	−66	−495	104	780	38	285
700	100	−57	−570	67	670	10	100
600	100	−49	−490	49	490	0	0
500	100	4	43	−16	−160	−12	− 117
400	100	0	0	−22	−220	−22	− 220
300	75	2	13	−4	−30	−2	−17
	$\sum_i(-\Delta p_i)\sum C_k r_k$		−6862	$\sum_i(-\Delta p_i)\sum_k C_k r_k$	+3412	$\sum_i(-\Delta p_i)\sum_L\sum_k C_k r_k$	−3450**
	Vapor convergence into updrafts ($\theta_E>345$K)		−6180†	Vapor divergence from downdrafts ($\theta_E<345$K)	+2730†		−3450**

* Units for columns 3, 5, 7 (m sec^{-1} gm kg^{-1}); for columns 4, 6, 8 (mb m sec^{-1} gm kg$^{-1}\times10$).

** Equivalent to a total net vapor convergence into the composite echo of 1.83×10^{13} gm.

† Obtained by overlaying the analyses of convergence, θ_E and r.

the data set (Table 2) calculated for the echo area:

$$\text{Mean rainfall per echo} = \frac{101}{90}\frac{A_R}{A_0} = 4.5 \text{ cm}.$$

This value is somewhat larger than the mesoscale budget value. The reason probably lies in the average values used for the mean echo (Table 1) for R, τ. There exists a size spectrum of echoes (Cruz, 1973) with some correlation between larger radius and longer lifetime. From (4.3) it can be seen that the net vapor convergence involves the product $R\tau$. Averaging over the whole data sample for the summer (about 230 echoes), we have

$$\overline{R\tau} = 1.1\bar{R}\,\bar{\tau}, \tag{5.1}$$

so that the use of average values $\bar{R}$, $\bar{\tau}$ may underestimate total echo rainfall by 10%. The same data gave

$$\overline{R^2} = 1.1(\bar{R})^2, \tag{5.2}$$

so that the comparison figures of rain per unit echo area of 550 km^2 become

Budget	3.7 cm
Measured	4.1 cm

which agree within experimental error.

In this paper only simple mean values $\bar{R}$, $\bar{\tau}$ have been used, although the correlation $\overline{R\tau}$ is clearly important to the interpretation of composite budgets. This requires further study.

d. Large-scale modification

No values for the synoptic-scale $\bar{\omega}$ are known since the experimental site in Venezuela is not within a good synoptic network. However, it is illuminating to calculate $\bar{\omega}$ (a mean value for the 17 days) using (4.10) and (4.11), from the cumulonimbus transports (the last column in Tables 5 and 7) and the mean change in $\bar{T}$, $\bar{r}$ (see Section 2f) over the period of deep convection,

TABLE 6. Synoptic-scale $\bar{\omega}$ calculation (in cgs units) from $\Delta\bar{T}$ [Eqs. (4.10) and (4.11)].

p (mb)	ΔT_{Cb} (°K)	$\frac{A_2\Delta\bar{T}}{A_1+A_2}$ (°K)	$\Delta T_{\bar{\omega}}$ (°K)	$(-\bar{\omega})_T$	$(-\bar{\omega}^*)_T$
950	−0.61				
900	−0.15				
850	0.30				
800	1.32	0.4	−0.9	0.81	37
700	1.18	0	−1.2	0.96	44
600	1.71	0	−1.7	1.14	52
500	1.95	−0.3	−2.3	1.53	70
400	2.44	−0.2	−2.6	1.88	87
300	2.88	+0.2	−2.7	2.34	107
250	2.08	+0.1	−2.0	2.08	95
200	2.02	−0.3	−2.3	2.28	104
175	1.26	−0.7	−2.0	1.11	51
150	−1.29	−1.1	−0.2	0.08	4

TABLE 7. Water vapor modification of the atmosphere.*

p (mb)	$\bar{r}^2$ (gm kg)$^{-1}$	V_1	V_2	V_1+V_2
990	(17.0)			
950	15.3	−80	−210	−290
900	13.7	−210	−300	−510
850	12.3	−305	−120	−425
800	10.6	−365	−30	−395
700	8.2	−450	−80	−530
600	5.0	−435	100	−335
500	2.7	−365	0	−365
400	1.2	−360	−10	−379
300	0.3	−220	−10	−230
250	0.1			
		Σ −2790	−660	−3450

* V_1, V_2 are the analogues of E_1, E_2 [see (4.6)] in units of 10 mb m sec^{-1} gm kg^{-1}.

while noting that (4.9) and (4.11) involve the assumption of no mean large-scale changes due to horizontal advection. The computation from the thermal changes is shown in Table 6. Two values are given: $\bar{\omega}_T$, a value for the mean time period Δt of deep convection, and $\bar{\omega}_T^*$ which is scaled to the area and half-lifetime of the composite so as to be directly comparable with $\sum_L \omega^*$. These are related as follows:

$$\bar{\omega} = \frac{NA_0\tau}{A_R\Delta t}\bar{\omega}^*.$$

The maximum value of $\bar{\omega}_T$ for the troposphere is about 2 cgs units, which is not unreasonable. The calculation is repeated in Tables 7 and 8 using water vapor changes to give $\bar{\omega}_r$ and $\bar{\omega}_r^*$. As stated in Section 2f the water vapor changes $\Delta\bar{r}$ are not considered very accurate. The values for $\bar{\omega}^*$ are plotted with $\sum_L \omega^*$ in Fig. 7. Within the errors the two values for $\bar{\omega}^*$ agree, except perhaps at 300–400 mb where the vapor calculation gives rather large values of $\bar{\omega}^*$. Evaporation from the surface may affect $\bar{\omega}_r^*$ at 950 mb, and radiation from anvil tops may mean that the peak in $\bar{\omega}_T^*$ at 200 mb is spurious.

Chiefly, one notes that $\bar{\omega}^*$ and $\sum_L \omega^*$ do not differ by much (see Section 6). However, between 700 and 300 mb the large-scale $\bar{\omega}^*$ is larger than the cumulonim-

TABLE 8. Synoptic-scale $\bar{\omega}$ calculation (in cgs units) from $\Delta\bar{r}$ [Eq. (4.11)].

p (mb)	Δr_{Cb} (gm kg^{-1})	$\frac{A_2\Delta\bar{r}}{A_1+A_2}$ (gm kg^{-1})	$\Delta r_{\bar{\omega}}$ (gm kg^{-1})	$(-\bar{\omega})_r$	$(-\bar{\omega}^*)_r$
950	−0.63	−0.25	0.38	0.60	28
900	−1.43	−0.84	0.59	0.82	38
850	−1.19	−0.67	0.52	0.67	31
800	−0.74	−0.34	0.40	0.62	29
700	−0.74	0	0.74	1.10	50
600	−0.47	0.34	0.81	1.24	57
500	−0.51	0.34	0.85	1.86	85
400	−0.52	0.34	0.86	2.98	136
300	−0.43	0.13	0.56	3.46	159

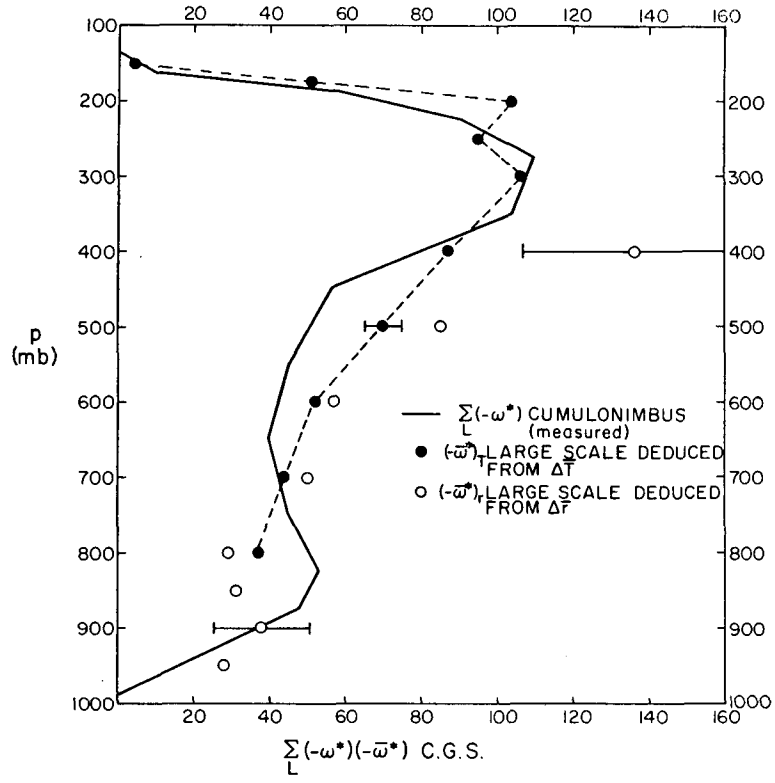

FIG. 7. Large-scale mean vertical mass flux, deduced from cumulonimbus budget and large-scale mean changes of temperature and mixing ratio. Error bars correspond to ± 0.1C in $\Delta\bar{T}$ and ± 0.2 gm kg^{-1} in $\Delta\bar{r}$.

bus scale $\sum_L \omega^*$. Thus, there is a residual upward motion in region 2 (the environment), producing a cooling and moistening, although at 600 mb the lifting is small and the cooling is cancelled here by a lateral transport of enthalpy out of the cloud region 1.

6. Discussion and conclusions

a. Mass transport models

Simple parameterizations of deep convection involving vertical mass transport (Riehl and Malkus, 1958; Pearce and Riehl, 1968; Ooyama, 1969, 1971; Yanai, 1971) and lateral mixing (Kuo, 1965) can be examined using (3.9), (3.10), (4.9), (4.11) and Tables 5 and 7. Clearly, the dominant terms are those in $\omega^*\partial\bar{\theta}/\partial p$ and $\omega^*\partial\bar{r}/\partial p$, i.e., the mass transport terms E_1 and V_1. For the heat balance the integrated "lateral" term ($\propto\sum_i E_2$) represents only 6% (190/3390 in Table 5) of the total enthalpy input, a result of near hydrostatic balance. For water vapor the corresponding vapor term ($\propto\sum_i V_2$) is rather larger, 19% (660/3450 in Table 7) of the total vapor convergence. Except for the surface levels 950–850 mb and at 150 mb, a simple mass transport model using ω^* and a mean atmosphere correctly represents about 90% of the cumulonimbus scale modification.

Since $\omega^*\approx\sum_L\omega^*$, one might approximately parameterize ω^* in terms of $\bar{\omega}^*$ and hence in terms of a low-level convergence (not necessarily frictionally induced as in CISK models). However, the low-level budgets cannot be expressed in terms of a single mass transport on the cumulonimbus scale, because cooling and drying are observed simultaneously. For example, one can define hypothetical mass fluxes Ω_T^*, Ω_r^* so that the cumulonimbus modifications are given by single terms involving the stratification and a mass flux, e.g.,

$$A_0\Omega_r^*\frac{\partial\bar{r}^{-2}}{\partial p}=A_0\omega^*\frac{\partial\bar{r}^{-2}}{\partial p}+\int_{l_1}C(r-\bar{r}^{-2})dl.$$

However, although Ω_T^*, Ω_r^* are comparable above 800 mb, they have opposite signs at the lowest levels. A detailed model of the surface (sub-cloud) layer is needed to accurately parameterize deep convection in terms of the large scale $\bar{\omega}$, not one based simply on mass flow into cumulonimbus updrafts.

The large-scale vapor convergence, calculated using $\bar{\omega}^*$ (from the water vapor budget between 850–950 mb and the thermal budget above) and $\bar{r}^2$, is 2930 units to be compared with the enthalpy source of 3390 units. Thus, synoptic-scale vapor convergence is a fairly close

measure of the heating of the atmosphere. With the mean sounding (Tables 5 and 7) and the 350K moist adiabat, Kuo's method, however, gives a precipitation only about one-quarter of the large-scale vapor convergence, with the remainder increasing the mean water vapor of the atmosphere. Thus, Kuo's method is a very poor estimate here of the total heating, and greatly overestimates the mean water vapor input to the convective layer.

b. *Factors influencing* ω^*

Accurate parameterization of ω^*, though necessary, is difficult, since the mean atmospheric changes $\Delta\bar{T}$, $\Delta\bar{r}$ (Tables 6 and 8) are small residuals, whose sign depends primarily on the detailed vertical structure of $\bar{\omega}$ and ω^*, and hence on the complex structure of updraft and downdraft, growth and decay. The factors controlling $\omega^*(p)$ are still not clearly resolved, but some may be suggested:

1) The large-scale shear field may control the organization of cloud systems as well as the updraft-downdraft patterns, and hence $\omega^*(p)$. It is hoped to investigate other classes of shear field than the one in this study in a future experiment. Most of the echo systems observed in this experiment did not seem well organized into patterns.

2) The transience of individual clouds is of importance. The cause may be the mid-level stabilization observed during the growth phase (+1K at 300–400 mb). However, again organization as well as storm propagation relative to low-level inflow and downdraft outflow may be significant.

3) The modification of the sub-cloud layer is undoubtedly significant. A model for this control (Betts, 1973) must, however, be extended to include moist downdrafts.

c. *Diurnal control*

During the experiment, the period of deep convection was transient (lasting about 6 hr) and linked to the diurnal cycle. This transience is clearly connected to the sub-cloud layer modification. Despite low-level convergence, and evaporation of rain from the surface, the sub-cloud layer dries significantly, and simultaneously is cooled. The corresponding stabilization and fall of θ_E is sufficient to terminate deep convection. Models for this sub-cloud layer process need to be developed, and are under investigation. The total 950-mb high θ_E (>345K) inflow for a convective episode corresponds to an area of 14,000 km^2 (as compared with a radar area of 20,000 km^2), while the corresponding synoptic-scale convergence is only about 4000 km^2. Thus, the deep convection appeared to end when about half the high θ_E surface layer had been "processed" by cumulonimbi.

d. *Conclusion*

Experimental results have been presented for a composite cumulonimbus system, and analyzed with a simple theoretical model. The usefulness of mass transport models is apparent as a simple representation of a model cumulonimbus, as are their inadequacies in the first 150 mb above the surface (corresponding with the sub-cloud layer region), where a more detailed model is necessary. Experimentally, the cumulonimbus transports under different synoptic conditions, particularly of wind shear, need to be investigated to identify the influence of large-scale parameters other than mean vertical motion.

Acknowledgments. The author acknowledges the foresight of Dr. H. Riehl in the design and execution of the experiment. The field experiment was supported by the Venezuelan Meteorological Service, and the Field Observing Facility and the Flight Facility of the National Center for Atmospheric Research. The cooperation and advice also of Mr. L. Cruz and Dr. K. Fraedrich in the analysis has been considerable. The research for VIMHEX I was sponsored by the Office of Naval Research under Contract N00014-68-A-0493-0002 with Colorado State University. Partial support for this theoretical analysis was received from the National Science Foundation under Grant GA-11637.

APPENDIX

T	temperature
θ	potential temperature
θ_E	equivalent potential temperature
p	pressure
r	water vapor mixing ratio
ρ	density
Q	a conserved quantity
∇	three-dimensional divergence operator
$\mathbf{v}$	vector wind
w	vertical velocity
ω	$-\rho g w$
g	acceleration due to gravity
C_p	specific heat of dry air
L	latent heat of vaporization of water
z	height coordinate
t	time

The model (see Fig. 1)

A_1	area: region 1 (contains echo)
A_2	area: region 2 (environment)
A_0	echo area
A_R	working area of radar
l_1	circumference of region 1 $[=4\pi R]$
l_2	circumference of region 2
Δl	$\pi R/3$
R	mean echo radius (used to scale $\hat{R}$)
$\hat{R}$	non-dimensional radius from echo center

C radial velocity on 1, 2 boundary (positive outward)
τ mean echo half-lifetime
N mean number of echoes per day
Δt mean length of echo period per day

Other symbols

$\tilde{(\ )}$ large-scale average (including several clouds and their environment)
$\tilde{(\ )}^1$ average over region 1 (model)
$\tilde{(\ )}^2$ average over region 2 (model)
$\bar{(\ )}$ large-scale and 17-day average [except in (5.1), (5.2)]
$\bar{(\ )}^1$ average over region 1 and 17 days data
$\bar{(\ )}^2$ average over region 2 and 17 days data
* a value of ω, scaled to the echo area A_0, and the echo half-lifetime τ
$'$ a deviation from an area-mean
Ω defined in (6.1)
$\sum_L$ a sum over lifetime of echo
$\sum_i$ a sum over pressure increments
$\sum_k$ a sum over 12 values on l_1
E_1, E_2, V_1, V_2 defined in text

REFERENCES

Betts, A. K., 1972: A composite mesoscale cumulonimbus budget. Atmos. Sci. Paper No. 186, Colorado State University.

——, 1973: Non-precipitating cumulus convection and its parameterisation. *Quart. J. Roy. Meteor. Soc.*, **99**, 178–196.

Cruz, L., 1973: Venezuelan rainstorms as seen by radar. *J. Appl. Meteor.*, **12**, 119–126.

Kuo, H. L., 1965: On formation and intensification of tropical cyclones through latent heat release by cumulus convection. *J. Atmos. Sci.*, **22**, 40–63.

Morrissey, J. F., and F. J. Brousaides, 1970: Temperature-induced errors in the ML-476 humidity data. *J. Appl. Meteor.*, **9**, 805–808.

Ooyama, K., 1969: Numerical simulation of the life cycle of tropical cyclones. *J. Atmos. Sci.*, **26**, 3–40.

——, 1971: A theory on parameterization of cumulus convection. *J. Meteor. Soc. Japan*, **49**, 744–756.

Pearce, R. P., and H. Riehl, 1968: Parameterization of convective heat and momentum transfer suggested by analysis of Caribbean data. *Proc. WMO-IUGG Symp. Numerical Weather Prediction*, Tokyo, Vol. 1, 75–84.

Rasmussen, J. L., R. W. Furman and H. Riehl, 1969: Moisture analysis of an extratropical cyclone. *Arch. Meteor. Geophys. Bioklim.*, **A18**, 275–298.

Riehl, H., and J. Malkus, 1958: On the heat balance of the equatorial trough. *Geophysica*, **6**, 503–537.

Yanai, M., 1971: A review of recent studies of tropical meteorology relevant to the planning of GATE. GATE Experiment Design Proposal, WMO-ICSU Annex I.